Hayden, A.T., Lamb, M.P., and Carney, A.J., 2021, Similar curvature-to-width ratios for channels and channel belts: Implications for paleo-hydraulics of fluvial ridges on Mars: Geology, v. 49, https://doi.org/10.1130/G48370.1

Data repository

This data repository contains description of previous work, our methods for curvature determination, a fractal geometry description of channel belts, martian ridge descriptions, and the measured data.

1. Prior methods for measuring curvature

The typical method to measure the planform geometry of a river channel has previously begun with manual definition of a line (Ferguson, 1975; Martin et al., 2018; Jacobsen and Burr, 2018). To capture river geometry efficiently, the line is typically digitized with a spacing between centerline points comparable to the channel width, though some studies use variable point spacing (e.g., Basher et al., 2018) and at least one study uses point spacing significantly smaller than channel width in their analysis of scroll-bar geometry (Jacobsen and Burr, 2018). Individual bends are defined either visually or algorithmically by places where the centerline changes direction (e.g., Ferguson, 1975; Williams, 1986; Kite et al., 2015). Meander half-wavelength, $\lambda/2$, is measured as the straight-line distance between bend termini, and arc wavelength (λ_a) is measured along the centerline. Within each bend, the radius of curvature is obtained by fitting a circle to the tightest point, which is known to have some variation between users (Williams, 1986), so sometimes measurements are repeated with different users (e.g., Kite et al., 2015; Jacobsen and Burr, 2018). Automated methods applied to these manually defined centerlines have also been used, including use of zero-crossings in planform geometry to determine ends of meander bends (Ferguson, 1975; Howard and Hemberger, 1991; Kite et al., 2015; Martin et al., 2018), and an automated circle-fitting algorithm (Jacobsen and Burr, 2018).

2. New method for measuring curvature

We developed a new method to analyze planform geometry that minimizes impact from the biases of manual centerline selection because channel belts have sinuous, non-parallel boundaries, and also minimizes impact from scale-dependent measurements that result from fractal geometry of river channels (e.g., Nikora, 1991) and channel belts.

The new method used a high-resolution trace of the landform outline as the input for all its analyses (Fig. DR1). The point spacing on the outline was smaller than the width of the landform by a factor 2 - 4 in order to reduce scale-dependent biases. The outline was then converted to a binary image mask and skeletonized to a centerline using RivMap, which employs Matlab image-processing tools to equally erode the shape laterally to find the centerline and discard any spurs that occur off the centerline (Schwenk et al., 2017). Widths were analyzed at every tenth pixel along the centerline by dividing the landform area parallel to that section of centerline by the length of that section of centerline (Schwenk et al., 2017), and then the median width, *W*, was taken for the whole landform.

The resulting high-resolution centerline was pixelated; to get a smoother centerline we generated a new centerline by resampling. To get the new centerline at arbitrary point spacing, η, we found the intersection of the original pixelated centerline and a circle of radius η drawn around the centerline start point, defined the next node in the new centerline at that intersection, and repeated the process along the entire length. We selected $\eta = W$ for our main scale of analysis.

Curvature (*C*) was calculated from its definition at each centerline node, using partial derivatives of latitude (*y*) and longitude (*x*) (where $x' = dx/\eta$ and $y'' = d^2y/\eta^2$, and each measurement is discrete) at each centerline position using actual coordinates and a η value (Vermeulen et al., 2016)

$$C = (x'y'' - x''y')/(x'^2 + y'^2)^{3/2} \quad \text{(DR1)}$$

Note that the line is made of discrete line segments, and so any method for determining curvature is limited. Schwenk et al. (2015) documented three different methods for determining curvature; the method we selected is their method 1. While they preferred method 3 for its built-in smoothing, it does this by approximating meander segments as circular arcs with constant curvature. We chose method 1 as it instead produces the maximal curvature at the apex of a second-order approximation, better aligning with prior work that manually fitted a circle to the tightest part of each bend.

With a series of curvature values at each centerline point, we then used zero-crossings in curvature to define the boundaries of bends, following prior methods (e.g., Vermeulen et al., 2016). For each bend, we took the inverse of the maximum curvature to get radius of curvature, R, for that bend, and found the straight-line distance between the bend termina as the meander half-wavelength, which we doubled to get wavelength, λ, similar to prior work (e.g., Kite et al., 2015). Automated methods detect many small-scale bends (e.g., Vermeulen et al., 2016), and we excluded bends made of one or two segments (along-centerline length $\leq 2\eta$) because such bends would be ignored in a visual analysis. This approach is similar to some prior work (e.g., Kite et al., 2015), which included a sinuosity threshold below which near-straight bends were incorporated into adjacent bends. We then took the median values of W, R, and λ from all included bends on the landform.

To assess the accuracy of our new method we compared it to the earlier manual method (Fig. DR2). We used the data from Williams (1986) for comparison, and applied our method to the listed rivers by tracing the river channels in Google Earth at the locations near the towns listed by Williams (1986). Discrepancies likely result because our method averages over a

number of bends, and it is unclear which bends Williams (1986) specifically studied. Furthermore, the tendency towards overestimating radius of curvature is likely due to the tendency of the algorithm to identify bends that are straighter than humans visually would include (Fig. DR1).

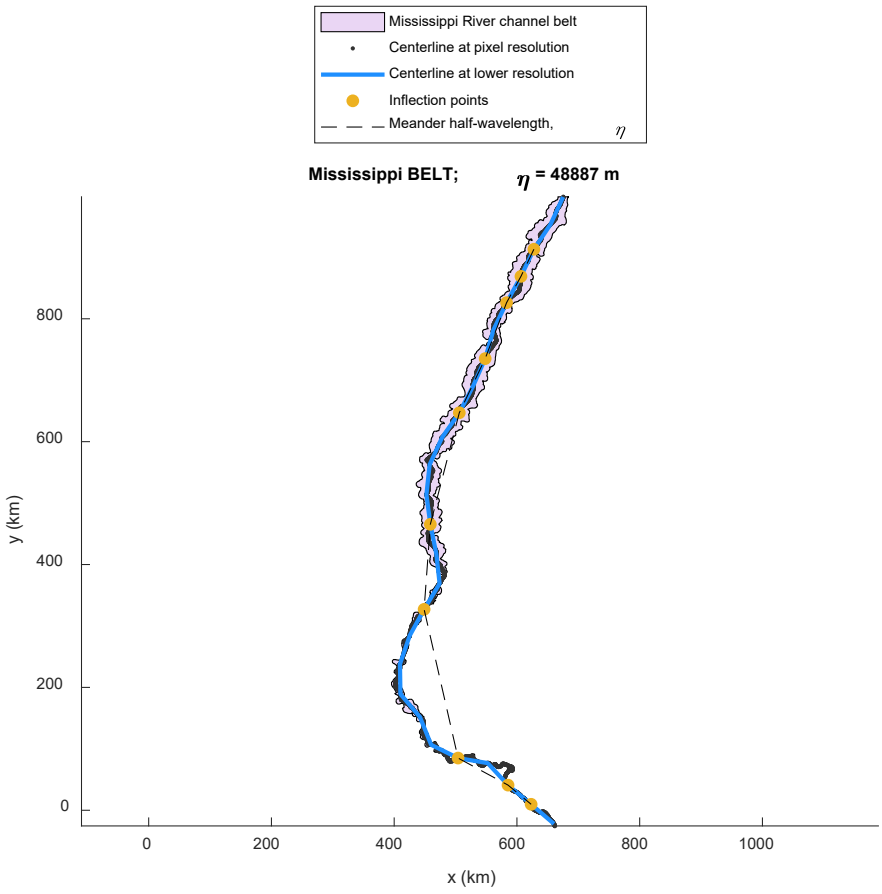

Fig. DR1—Automated analysis on the channel belt of the Mississippi River (blue shape) captures the centerline at a variety of scales and calculates wavelength for all bends at each scale. The solid black line is all the points recognized by the RivMap algorithm (Schwenk et al., 2017) as the centerline at pixel-scale resolution, while the blue line is the centerline resampled at lower resolution, η. The resampling loses details finer than η but captures larger-scale features. Yellow points are the bend inflection points detected on the blue line, and the dashed black lines connect them and thereby represents the half-wavelength of each bend.

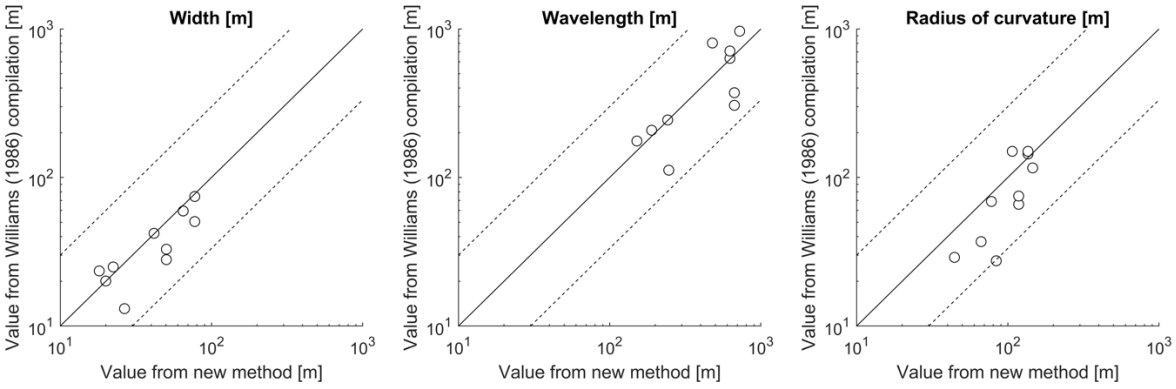

Fig. DR2.--Comparison between values from Williams (1986) and values from our new method, using $\eta = W$ to emulate the manual methods. Dashed lines represent a factor of three difference.

3. Kolmogorov-Smirnov similarity testing

To evaluate the similarity of the distributions of wavelength-width and radius-of-curvature-width ratio, we used two-factor Kolmogorov-Smirnov tests (*kstest2* in Matlab). This analysis computes the difference between the cumulative distribution functions (CDFs) of each parameter and uses the maximum difference between the CDFs to evaluate the probability that each set of values were drawn from the same distribution. We used $p < 0.05$ as the threshold to reject the null hypothesis that values were drawn from the same distribution, where the value of p is the probability an observed test statistic will be at least as extreme as the observed value under the null hypothesis. Comparing the landforms pairwise for λ/W, we rejected the null hypothesis (i.e., values are likely from different distributions) for channels and belts ($p = 0.002$) and ridges and belts ($p = 0.01$), while we failed to reject the null hypothesis (i.e., values are likely from the same distribution) for channels and ridges ($p = 0.07$). Comparing the landforms pairwise for R/W, we failed to reject the null hypothesis for channels and belts ($p = 0.14$), channels and ridges ($p = 0.77$), and ridges and belts ($p = 0.57$).

4. Fractal nature of channels, channel belts, and ridges

River channel planview curvature can be described using fractal geometry (Mandelbrot, 1982; Nikora, 1991; Montgomery, 1996), and we hypothesized that fractal geometry plays a role in setting the wavelength and radius of curvature for channels and channel belts. Here, we tested the hypothesis that channel belts are fractal like river channels.

The fractal equation relates the straight-line distance between endpoints (L_0) to the length of the curve (L_η) measured at arbitrary node spacing η (Mandelbrot, 1982)

$$L_\eta / \eta = (L_0 / \eta)^F \quad \text{(DR2)}$$

in which F is the fractal dimension. A non-fractal plane curve will have F=1, and F>1 is indicative of fractal behavior. We determined F using a Richardson plot, which relates the length of a sinuous line to the scale at which is measured (centerline node spacing, η), in which the slope of the best-fit line is equal to 1-F (Fig. DR3).

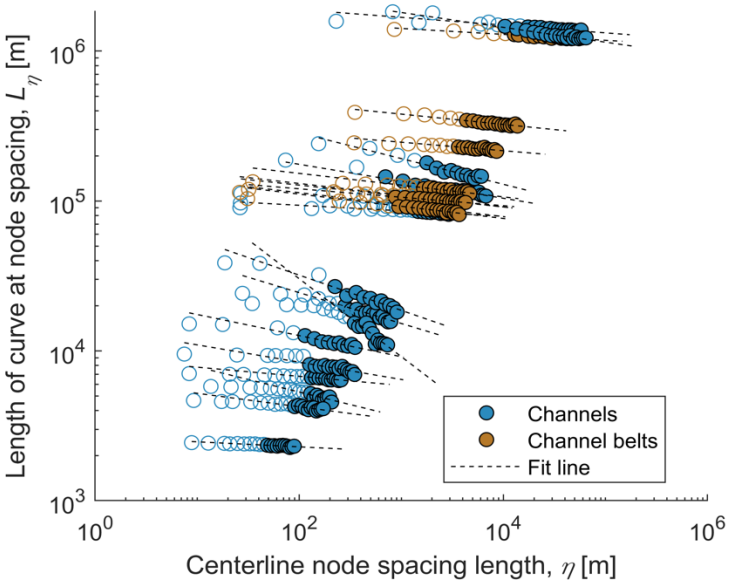

Fig. DR3–Richardson plots for each terrestrial location analyzed. Each data has a section where L_η is mostly independent of η (empty circles) and a section where L_η scales as η to a negative power (filled circles). The scale-dependence of length is a fractal property, so any feature that shows this dependence is fractal. Slope of the best-fit line (i.e., the exponent of a power-law fit;

dashed line) is equal to $1 - F$. Small scales are non-fractal. The steepest line is for the Murrumbudgee River, which has the highest fractal dimension ($F = 1.52$).

We found that channels in our database have fractal dimensions between 1.03-1.52, similar to previous work 1.1-1.5 (Montgomery, 1996). We detected rollover points from the data on Fig. DR3 using the *findchangepts* command in Matlab, which determines which subset of points have a stable mean value and which points destabilize that mean. The rollover observed with this method (open circles in Fig. DR3) indicates a minimum scale of fractal geometry, which Nikora (1991) predicted to be near the channel width. However, unlike the predictions of Nikora (1991), we did not observe any rollover at large scale on the Richardson plot that would indicate upper limits on the fractal behavior of channels, such as bounds from a confining valley.

Channel belts also follow fractal scaling, but have generally smaller fractal dimensions of 1.04-1.08 (Fig. DR3). Similar to our observations of the river channels, the fractal behavior of channel belts also is bounded at the smallest scales. The low values of fractal dimension for channel belts are likely related to the relatively low sinuosity of channel belts compared to channels because sinuosity and fractal dimension are related (Montgomery, 1996).

Since individual channels and channel belts exhibit fractal dimensions $F>1$ down to a scale near that of their width, both exhibit curves at scales down to the width. Thus, both have ratios of wavelength-to-width and radius of curvature-to-width near the lower bounds defined by Eqs. (3) and (4). It may be possible in some instances to identify channel belts by their lower fractal dimensions, but the wide range of dimensions for channels make this metric ambiguous.

5. Mars ridges analyzed

Martian ridges included in the study are shown below (Figs. DR4-DR11). In all images, the background is the CTX mosaic (Malin et al., 2007; Dickson et al., 2018), analyzed ridge(s) are traced in red, the prior centerline sketch of Kite et al. (2019) is in orange when available, and coordinate of location from Burr et al., (2009) is also given. In the numerous cases where other ridges are present they are indicated with arrows. Illustrations of the measurement are also provided; in all illustrations the red shape is the traced landform from CTX images, black solid line is the skeletonized centerline at pixel resolution, light blue line is the centerline rescaled to node spacing of $\eta = W$, yellow dots are the inflection points identified by the curvature analysis, and black dashed line is the meander half-wavelength. In some cases, the algorithm finds so many inflection points that the whole line appears yellow; these occur when the landform is made of many segments, and the algorithm detects the many small curves rather than focusing on the large curves that are visually prominent, which is due to the fractal or multiscale.

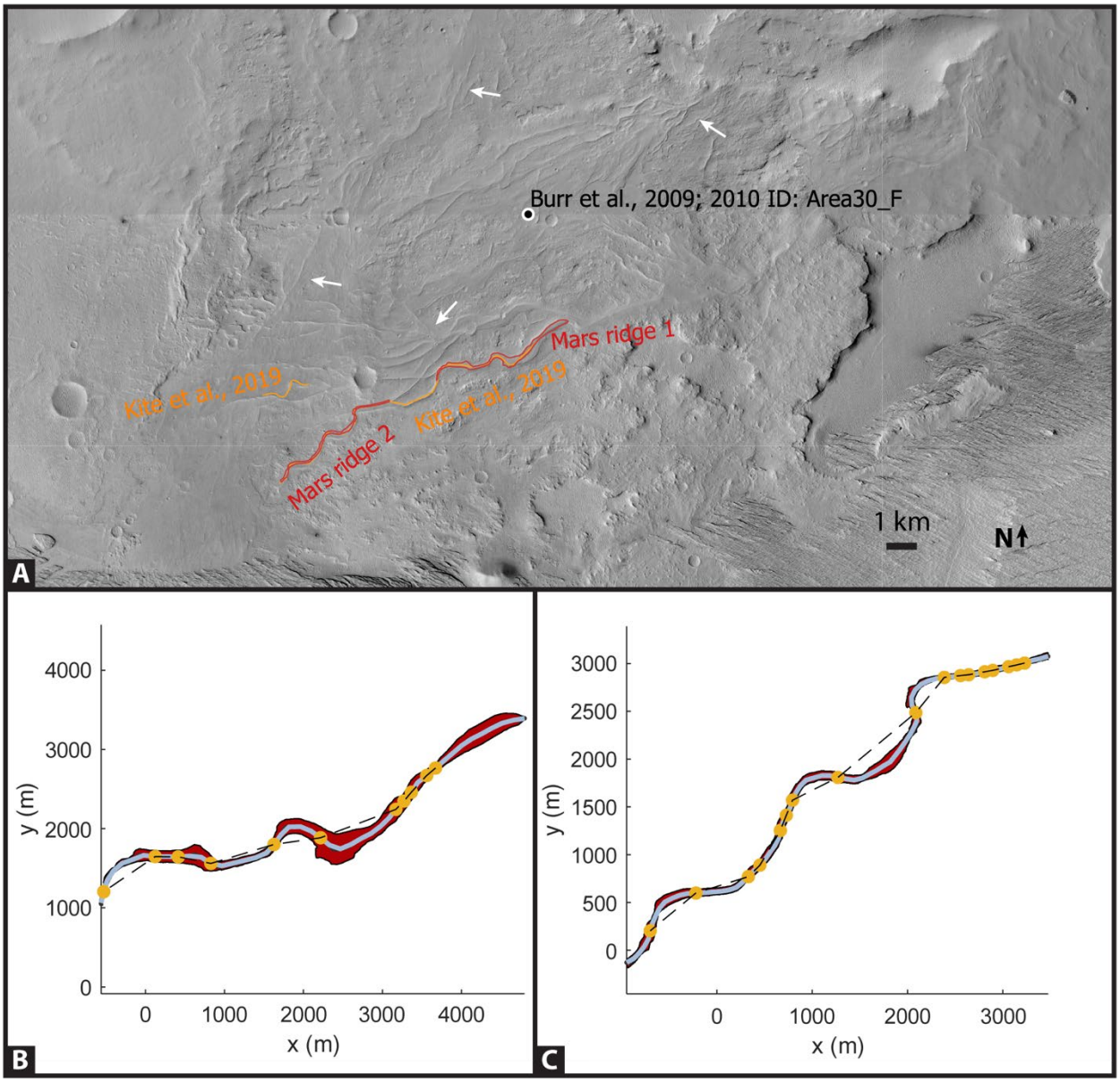

Fig. DR4 – Mars Ridges 1 and 2, which were noted by Burr et al. (2009) and previously analyzed by Kite et al. (2019). A) Numerous ridges are present in northeast Aeolis Dorsa (153.7ºE, -4.1ºS). We studied one ridge studied by Kite et al. (2019), but we split it into two because the ridge width changes visibly at a bifurcation that occurs between our two segments. Numerous other ridges are present (white arrows), and stacking patterns are clear (see also Fig. 1). B) Ridge 1, analyzed at $\eta = 146$ m. C) Ridge 2, analyzed at $\eta = 86$ m.

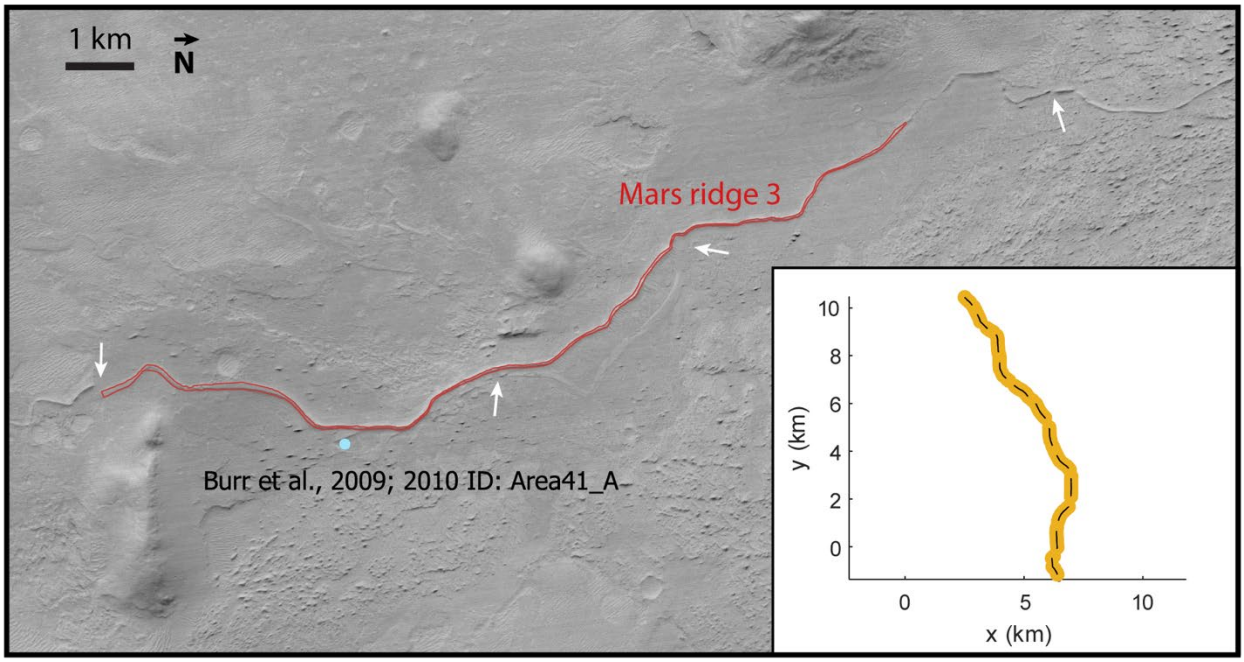

Fig. DR5 – Mars Ridge 3, which was noted and analyzed by Burr et al. (2009; 2010) in central Aeolis Dorsa (152.7ºE, 5.7ºS). Other ridges are present, and white arrows here indicate locations where stacked ridges cross (see also Fig. 1). Inset: sketch of Ridge 3, analyzed at $\eta = 38$ m.

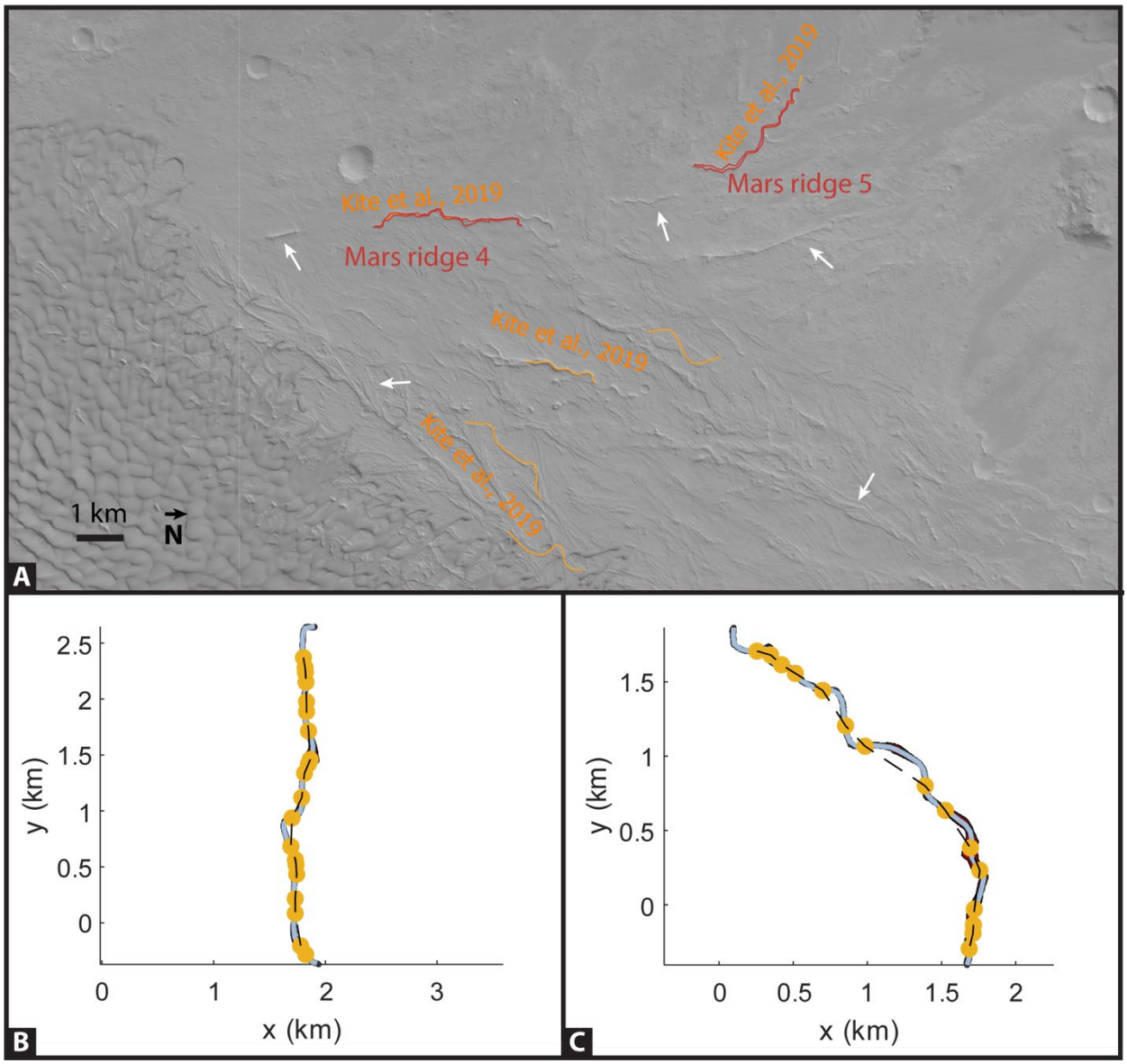

Fig. DR6 – Mars Ridges 4 and 5, which were previously analyzed by Kite et al. (2019). A) Numerous ridges are present in Roddy Crater. We studied two ridges previously studied by Kite et al. (2019), and numerous other ridges are present (white arrows). Stacking patterns are clear. B) Ridge 4 (39.76°W, 21.65°S), analyzed at $\eta = 44$ m. C) Ridge 5 (39.79°W, 21.54°S), analyzed at $\eta = 56$ m.

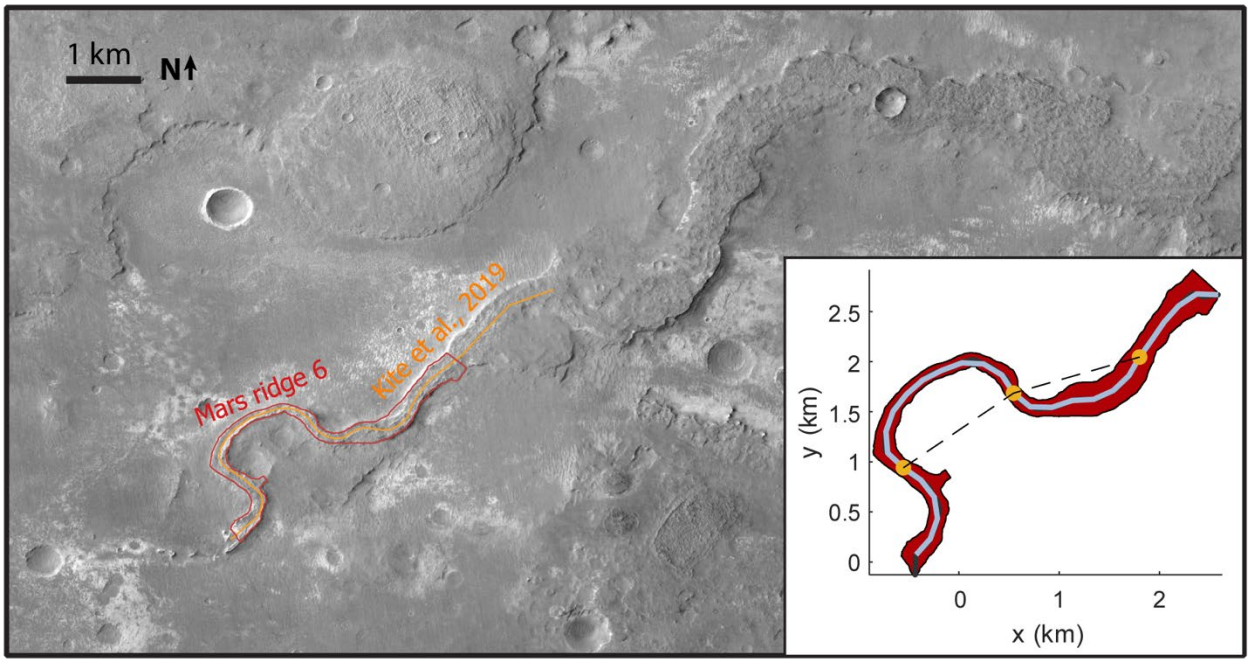

Fig. DR7 – Mars Ridge 6, which was noted and analyzed by Kite et al. (2019) in northern Greely Crater (2.77°E, 34.23°S). The ridge extends further to the right in the image, but becomes complicated by impact craters so we only analyzed a subset, like Kite et al. (2019). Inset: sketch of Ridge 6, analyzed at $\eta = 215$ m.

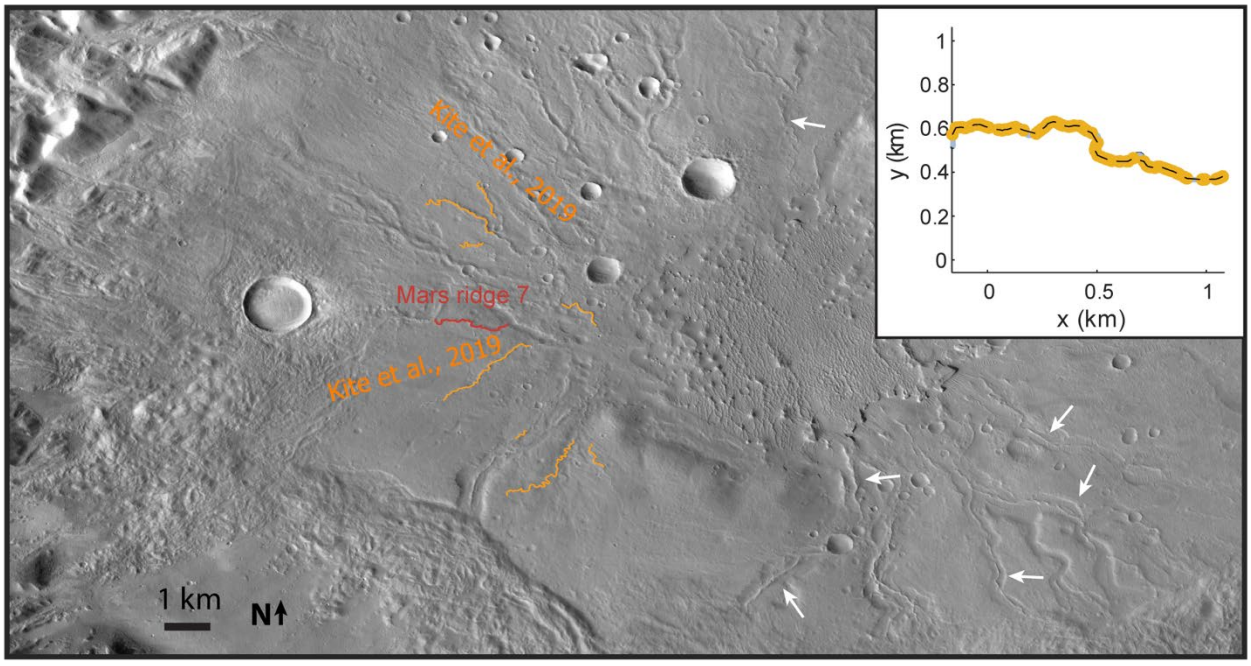

Fig. DR8 – Mars Ridge 7, which was noted and analyzed by Kite et al. (2019) in Chukhung Crater (72.58ºW, 38.465ºN). Other ridges are present (white arrows). Inset: sketch of Ridge 7, analyzed at $\eta = 7$ m.

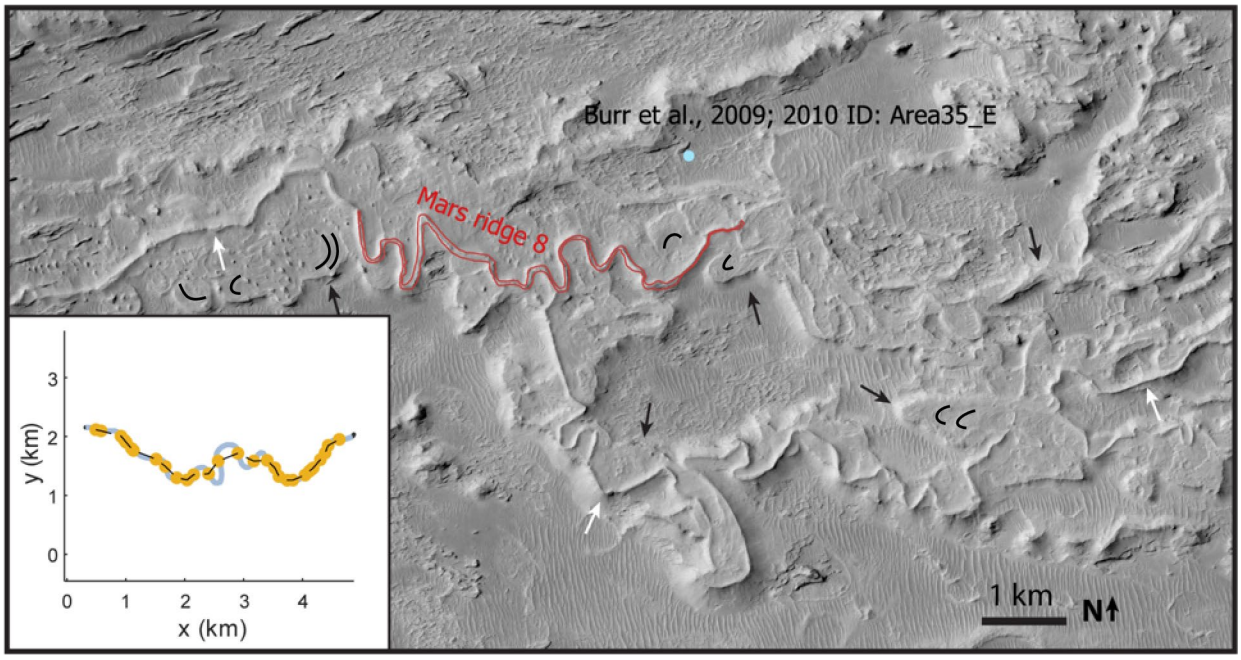

Fig. DR9 – Mars Ridge 8, which was noted and analyzed by Burr et al. (2009; 2010) in eastern Aeolis Dorsa (154.878ºE, 4.92ºS). Numerous other ridges are present, and white arrows here indicate those that were interpreted as inverted channels while black arrows indicate those interpreted as exhumed channel belts (Burr et al., 2009; 2010), due in part to lateral accretion sets visible at higher resolution (black arcs). Inset: sketch of Ridge 8, analyzed at $\eta = 60$ m.

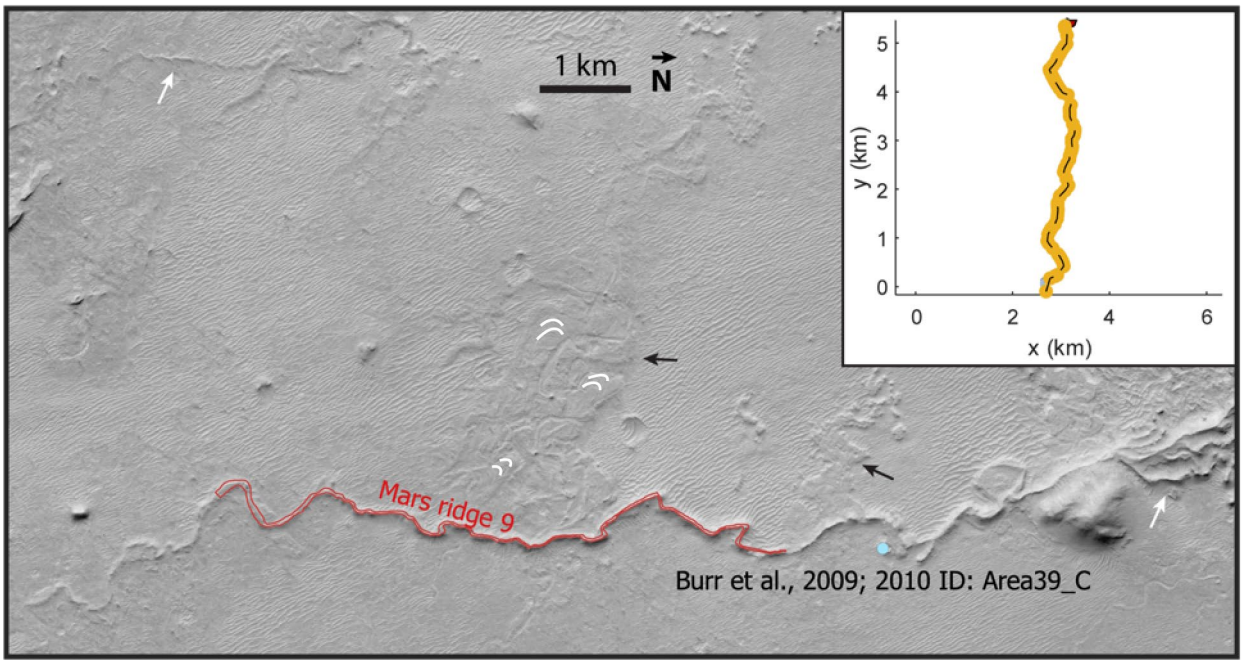

Fig. DR10 – Mars Ridge 9, which was noted and analyzed by Burr et al. (2009; 2010) in southeastern Aeolis Dorsa (153.59ºE, 6.3ºS). A few other ridges are present (white arrows), and there appear to be lateral accretion sets indicating channel belts (black arrows/white arcs). Inset: sketch of Ridge 9, analyzed at $\eta = 28$ m.

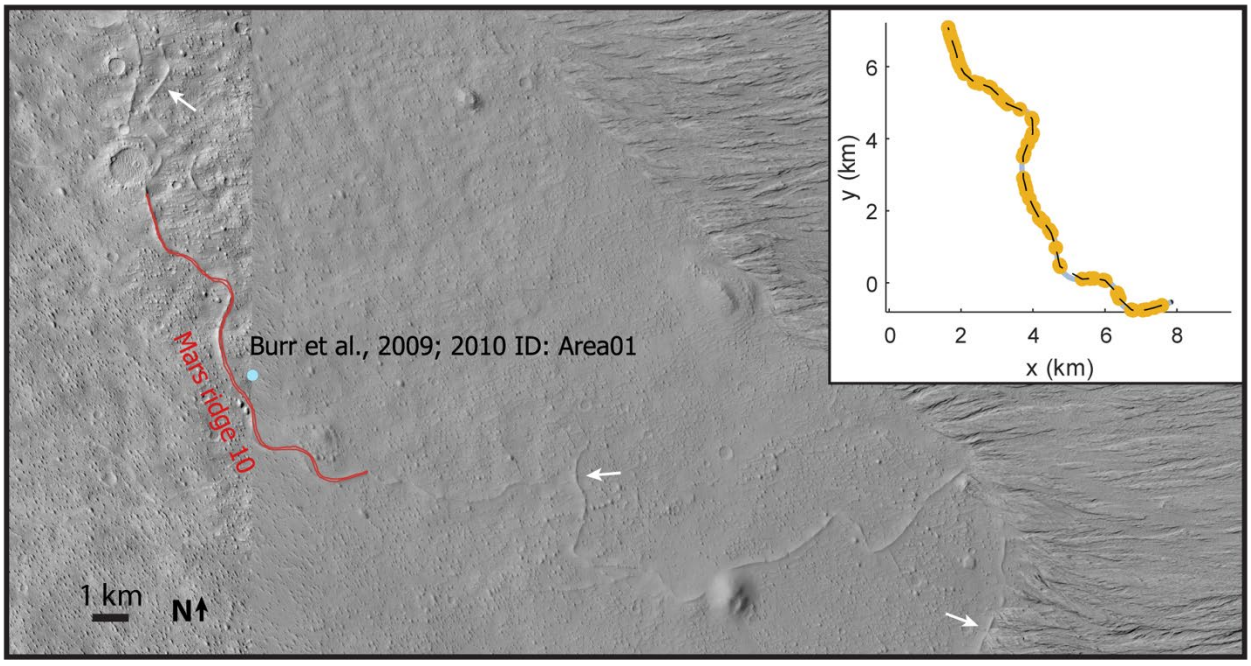

Fig. DR11 – Mars Ridge 10, which was noted and analyzed by Burr et al. (2009; 2010) in northeast Aeolis Dorsa (151.99ºE, 2.9ºS). Other ridges are present (white arrows). Inset: sketch of Ridge 10, analyzed at $\eta = 55$ m.

Landform Name	**Location**	**Original centerline node spacing, η (m)**	**Node spacing at analysis scale, $\eta \approx W$ (m)**	**Width, W (m)**	**Half-wavelength, $\lambda/2$ (m)**	**Meander arc length (m)**	**Radius of curvature, R (m)**	**Sinuosity, S (-)**	**Length, L_η, measured at $\eta = W$ (m)**	**Fractal dimension, F**	**Number of bends analyzed**
Assiniboine River [a]	50.04N, 97.88W	3.67	73.5	74.3	440	515	287	1.94	187000	1.11	259
Desna [b]	51.0N, 30.9E	17.9	155	153	991	1240	431	1.82	241000	1.17	154
Emån [b]	57.41N, 15.62E	1	18.5	18.5	90.8	92.3	75.6	1.32	2420	1.03	17
Lagan [b]	57.19N, 14.05E	4.23	21.5	22.4	121	139	77.9	1.71	5750	1.17	32
Lesser Slave River [b]	55.2N, 114.1W	3.3	65.6	65	362	525	146	1.69	24000	1.21	42
Ljusnan [b]	62.55N, 12.57E	0.886	28.5	26.6	123	142	83.9	1.36	6980	1.06	37
Logdealven [b]	65.14N, 20.73E	0.849	48.9	50.3	334	538	118	2.01	9330	1.12	16
MacKenzie River [a]	65.5N, 127.7W	26.2	1490	1520	5830	5950	5960	1.32	1550000	1.05	175
Mississippi BELT [c]	33N, 91W	237	24900	24500	91000	99500	99600	1.23	1240000	1.04	6
Mississippi CHANNEL [c]	33N, 91W	236	2030	2040	7530	10100	3780	1.75	1800000	1.1	153
Murrumbidgee River [b]	34.5S, 144.8E	9.86	75.3	77.5	312	452	136	2.36	20300	1.52	39
Rhine Belt 1 [d]	52.00N, 5.10E	100	1050	1060	3670	4220	2360	1.74	382000	1.07	65
Rhine Belt 1 CHANNEL [b]	52.00N, 5.10E	3.56	170	167	901	935	857	1.19	109000	1.07	74
Rhine Belt 2 [d]	51.87N, 6.01E	50	1660	1690	4890	4990	3490	1.16	238000	1.06	24
Rhine Belt 2 CHANNEL [b]	51.87N, 6.01E	3.57	297	292	1770	1780	1910	1.16	92500	1.08	34

Rhine Belt 3 [d]	51.83N, 5.55E	3.57	636	556	2380	2860	1430	1.25	111000	1.08	28
Rhine Belt 3 CHANNEL [b]	51.83N, 5.55E	3.57	132	129	790	793	942	1.23	89000	1.04	61
Svagan [b]	61.90N, 16.52E	1.07	22.2	20	94.8	111	66.6	1.41	4600	1.09	28
Swan River [b]	55.3N, 115.4W	2.15	41.1	41.7	239	329	107	2.79	38400	1.23	96
Tomichi Creek [b]	38.53N, 106.93W	2.45	17.8	18.1	75.7	88.9	44.4	1.65	15000	1.14	119
Vermont Belt 1 BELT [e]	43.84N, 73.15W	9.44	446	491	1570	1780	1140	1.21	130000	1.08	47
Vermont Belt 2 BELT [e]	44.4N, 73.0W	9.41	218	211	653	871	562	1.47	115000	1.06	81
Vermont Belt 3 BELT [e]	44.65N, 72.94W	4.09	247	244	749	989	593	1.33	99900	1.08	61
Mars ridge 1 [f,g]	4.10S, 153.79E	3.9	179	180	850	894	311	1.11	6440	1.04	3
Mars ridge 10 [g]	2.9S, 151.99E	3.91	54.6	58.2	271	273	396	1.21	12000	1.03	28
Mars ridge 2 [f,g]	4.17S, 153.65E	3.9	76.4	77.7	439	459	303	1.13	6110	1.02	11
Mars ridge 3 [g]	5.7S, 152.7E	1.95	38.3	37.6	133	134	263	1.13	14100	1.07	46
Mars ridge 4 [f]	21.65S, 39.76W	1.95	39.6	41.4	165	198	162	1.11	3320	1.03	11
Mars ridge 5 [f]	21.54S, 39.79W	3.75	43.1	49.3	172	194	113	1.22	3360	1.04	10
Mars ridge 6 [f]	34.23S, 2.77E	3.58	215	210	1320	1830	399	1.46	5800	1.02	2
Mars ridge 7 [f]	38.465N, 72.58W	0.792	16	15.8	63.3	64.1	38.4	1.28	2040	1.12	21
Mars ridge 8 [g]	4.92S, 154.878E	3.88	49.1	52.2	215	295	99.3	1.85	9340	1.14	24
Mars ridge 9 [g]	6.3S, 153.59E	1.95	27.7	27.7	108	111	95.4	1.22	6870	1.06	38

Table DR1—Data from study. Mask pixel size and point spacing are user-specified; all other values result from the automated analyses. Data are plotted in Fig. 3. Data sources: [a] shapefiles North American Water Polygons (Esri; downloaded from arcgis.com), rivers selected for their large size; [b] shapefiles downloaded from OpenStreetMap (www.openstreetmap.org) using the “overpass turbo” application of

Overpass API (http://overpass-turbo.eu); [c] Shapefile from Fernandes et al. (2016); [d] shapefiles from Digitaal Basisbestand Paleogeografie van de Rijn-Maas Delta (Cohen and Stouthamer, 2012); [e] shapefiles from Vermont Department of Environmental Quality maps of "river corridors", which they define as including "the width of the meander belt of a river and an additional 50' buffer" (https://dec.vermont.gov/watershed/rivers/river-corridor-and-floodplain-protection/river-corridor-and-floodplain-maps); [f] shapefile traced on Context Camera imagery in Google Mars, selected from ridges interpreted as inverted channels in Kite et al. (2019); [g] shapefile traced on Context Camera imagery in Google Mars, selected from ridges interpreted as inverted channels in Burr et al. (2009, 2010), specifically, their areas 01, 30_F, 35_E, 39_C, and 41_A

Works cited in supplement

Basher, Z., Lynch, A. J., and Taylor, W. W., 2018, New global high-resolution centerlines dataset of selected river systems: Data in brief, v. 20, p. 1552-1555. doi: 10.1016/j.dib.2018.09.016.

Burr, D. M., Enga, M.-T., Williams, R. M. E., Zimbelman, J. R., Howard, A. D., and Brennand, T. A., 2009, Pervasive aqueous paleoflow features in the Aeolis/Zephyria Plana region, Mars: Icarus, v. 200, no. 1, p. 52-76. doi: 10.1016/j.icarus.2008.10.014.

Burr, D. M., Williams, R. M. E., Wendell, K. D., Chojnacki, M., and Emery, J. P., 2010, Inverted fluvial features in the Aeolis/Zephyria Plana region, Mars: Formation mechanism and initial paleodischarge estimates: Journal of Geophysical Research: Planets, v. 115, no. E07011. doi: 10.1029/2009JE003496.

Dickson, J. L., Kerber, L. A., Fassett, C. I., and Ehlmann, B. L., A global, blended CTX mosaic of Mars with vectorized seam mapping: a new mosaicking pipeline using principles of non-destructive image editing, *in* Proceedings Lunar and Planetary Science Conference2018, Volume 49.

Ferguson, R. I., 1975, Meander irregularity and wavelength estimation: Journal of Hydrology, v. 26, no. 3-4, p. 315-333.

Howard, A. D., and Hemberger, A. T., 1991, Multivariate characterization of meandering: Geomorphology, v. 4, no. 3-4, p. 161-186.

Jacobsen, R. E., and Burr, D. M., 2018, Errors in Martian paleodischarges skew interpretations of hydrologic history: Case study of the Aeolis Dorsa, Mars, with insights from the Quinn River, NV: Icarus, v. 302, p. 407-417. doi: 10.1016/j.icarus.2017.11.014.

Kite, E. S., Howard, A. D., Lucas, A., and Lewis, K. W., 2015a, Resolving the era of river-forming climates on Mars using stratigraphic logs of river-deposit dimensions: Earth and Planetary Science Letters, v. 420, p. 55-65. doi: 10.1016/j.epsl.2015.03.019.

Kite, E. S., Mayer, D. P., Wilson, S. A., Davis, J. M., Lucas, A. S., and de Quay, G. S., 2019, Persistence of intense, climate-driven runoff late in Mars history: Science Advances, v. 5, no. 3, p. eaav7710. doi: 10.1126/sciadv.aav7710.

Malin, M. C., Bell, J. F., Cantor, B. A., Caplinger, M. A., Calvin, W. M., Clancy, R. T., Edgett, K. S., Edwards, L., Haberle, R. M., James, P. B., Lee, S. W., Ravine, M. A., Thomas, P. C., and Wolff, M. J., 2007, Context Camera Investigation on board the Mars Reconnaissance Orbiter: Journal of Geophysical Research, v. 112, no. E5. doi: 10.1029/2006je002808.

Mandelbrot, B. B., 1983, The fractal geometry of nature, WH freeman New York.

Martin, J., Fernandes, A. M., Pickering, J., Howes, N., Mann, S., and McNeil, K., 2018, The Stratigraphically Preserved Signature of Persistent Backwater Dynamics in a Large Paleodelta System: The Mungaroo Formation, North West Shelf, Australia: Journal of Sedimentary Research, v. 88, no. 7, p. 850-872. doi: 10.2110/jsr.2018.38.

Montgomery, K., 1996, Sinuosity and Fractal Dimension of Meandering Rivers: Area, v. 28, no. 4, p. 491-500.

Nikora, V. I., 1991, Fractal structures of river plan forms: Water resources research, v. 27, no. 6, p. 1327-1333.

Schwenk, J., Lanzoni, S., and Foufoula-Georgiou, E., 2015, The life of a meander bend: Connecting shape and dynamics via analysis of a numerical model: Journal of Geophysical Research: Earth Surface, v. 120, no. 4, p. 690-710. doi: 10.1002/2014JF003252.

Schwenk, J., Khandelwal, A., Fratkin, M., Kumar, V., and Foufoula-Georgiou, E., 2017, High spatiotemporal resolution of river planform dynamics from Landsat: The RivMAP toolbox and results from the Ucayali River: Earth and Space Science, v. 4, no. 2, p. 46-75. doi: 10.1002/2016EA000196.